Materials Today: Proceedings 62 (2022) 7759–7766

Contents lists available at ScienceDirect

Materials Today: Proceedings

journal homepage: www.elsevier.com/locate/matpr

OER/ORR parameters of Fe^{2+} and Co^{2+}-doped manganese dioxide electrode materials

Luiza Zudina [a,b], Georgii Sokolsky [c,a,*], Vitalii Chumak [a], Nadiia Haiuk [a,d]

[a] National Aviation University, Huzara ave. 1, Kyiv 03058, Ukraine
[b] Separate Structural Subdivision "Sumy Professional College" of the National University of Food Technologies, Sumy Region, Sumy, Street Yaroslav the Wise, 60, 40000, Ukraine
[c] National Technical University of Ukraine "Igor Sikorsky Kiev Politechnic Institute", Peremohi Ave. 37, 03056 Kyiv, Ukraine
[d] Bila Tserkva National Agrarian University, pl. Soborna 8/1, 09117, Kyiv Region, Bila Tserkva, Ukraine

ARTICLE INFO

Article history:
Available online 9 June 2022

Keywords:
Manganese dioxide
Electrolytic doping
Electrocatalyst
Oxygen reduction reaction
Oxygen evolving reaction
Hollandite

ABSTRACT

The system of cationic additives [M(I) = NH_4^+; M(II) = Co^{2+}, Fe^{2+}] in electrodeposition electrolytes of manganese dioxide was used to directly modify its electrocatalytic activity in oxygen reduction and oxygen evolving reactions (ORR & OER) in 0.3 M KOH. Doped MnO_2 products were characterised by AAS, SEM with EDS, XRD, TGA, and FTIR. The correlations of ORR(OER) parameters with the content of dopant ions were established, bifunctionality analysis of obtained doped materials was made.

1. Introduction

Bifunctionality of electrode materials is the intensively studied concept nowadays focused on application in Li-air batteries (LAB) [1–7]. Despite the significant efforts made since the LAB first mention and the large number of publications [7], this system is far from commercialization, potential electrode material candidates are still under study. The sluggish kinetics of the oxygen reduction reaction (ORR) limits the efficiency of numerous oxygen-based energy conversion devices such as fuel cells and metal-air batteries.

Among other widespread oxides on Earth, manganese-based oxide electrocatalysts exhibit activity close to the activity of noble metals [8]. The lower overpotential and the higher current densities at the given electrode potential the more prospective are the electrode materials considered for ORR/OER application [9].

The structure and physicochemical properties of manganese dioxide are predetermined by synthetic procedures: chemical (chemical manganese dioxide (CMD)) or electrochemical ones. Electrochemical manganese dioxide (EMD) of the so-called γ-MnO_2 polymorph possesses such structural features as high concentration of ramsdellite/pyrolusite intergrowths [10], Mn^{3+}/Mn^{4+} pairs in the same sites of crystal lattice, cationic vacancies, etc. As shown in [11], EMD containing α-MnO_2 polymorph can be obtained by electrolytic doping method.

The large ORR/OER overpotentials reduce the LAB cycle life and limit its capacity [12,13]. Therefore, it is critical to develop suitable electrocatalyst to address the issue. Platinum is still the most active ORR/OER catalyst. Commercial applications of Pt-based catalysts are limited by the high cost and the susceptibility to poisoning [14]. The interest to manganese(IV) oxide system has grown significantly after the pioneering works of P. Bruce [15]. As shown in [15], α-MnO_2 is one of the most active ORR/OER electrocatalysts.

Composition, structure, and properties of EMDs depend strongly on the nature of an electrolyte. The tool to influence the activity of manganese(IV) oxide is the doping by other cations [3]. EMDs of hollandite or α-MnO_2 polymorph structure can be obtained by electrolytic doping of an electrolyte with M^+–ions (M = Li, Na, K, NH_4) [16]. EMD samples containing additives of Co^{2+}, Fe^{2+} were obtained by the method of electrolytic doping earlier in our group [17,18]. The advantages of monodoped by Cobalt (II) or Iron(II) EMDs in ORR were also established in [4]. Composition and properties of EMDs obtained from fluoride-containing electrolytes can be easily controlled [19]. Electrodeposition products can be produced at higher rates due to increased mobility of fluoride-containing coordination compounds of manganese(II) in these electrolytes [20].

* Corresponding author at: National Technical University of Ukraine "Igor Sikorsky Kiev Politechnic Institute", Peremohi Ave. 37, 03056 Kyiv, Ukraine.
E-mail addresses: georgii.sokolsky@gmail.com, g.sokolsky@kpi.ua (G. Sokolsky).

https://doi.org/10.1016/j.matpr.2022.05.570

The aim of this study was to investigate kinetic parameters of ORR/OER on Fe^{2+}, Co^{2+}- co-doped EMDs electrode materials synthesized from F^-, Fe^{2+} and Co^{2+}-containing electrolytes with M = NH_4^+-ions as α-MnO_2 polymorph templates to analyse influence of various factors on the activity of doped samples.

2. Experimental

Manganese(IV) oxide samples were electrodeposited galvanostatically (i = 10 A/dm^2) on Pt anode. The pristine fluoride-containing electrolyte consisted of 0.1 M HF + 0.7 M $MnSO_4$ and the dopant additives in the electrolyte were sulfates of the following cations in different concentrations: NH_4^+, Fe^{2+}, Co^{2+} [20].

The dopants concentrations were chosen taking into account solubility of these compounds, their electrochemical behaviour, i.e. the ability to be incorporated into deposit in minor amounts, and also the preliminary experimental results. Electrolytic doping by Fe^{2+} and Co^{2+} of EMDs included the binary or trinary cationic additives to affect the phase composition and functionality of the electrodeposition product (Table 1). The additives of cations in the following concentrations were used: 0.01 or 0.1 M (Co^{2+}, Fe^{2+}), and 1.5 M (NH_4^+).

Deposits were separated by decantation and filtration after electrodeposition experiment, rinsed with distilled water till the negative reaction on $BaCl_2$, dried 3 h at 110 °C to eliminate physically sorbed water.

The following methods were used for characterization of samples: voltammetry; atomic absorption spectrometry (AAS) and thermogravimetry (Q-1000, IOM, Hungary); energy-dispersive X-ray fluorescence (mobile precision analyzer Expert 3L); X-ray diffraction method (DRON-4, Russia, MoKα, CuKα – irradiation); scanning electron microscopy (Tescan Mira 3 LMU, Czechia); infrared Fourier spectroscopy (FSM 1201, St. Petersburg, Russia). For determining the BET surface N_2 physisorption experiments were performed with a Autosorb-6B (Quantachrome instruments, USA) after degassing the samples at 180 °C for 20 h.

Electrochemical experiment was carried out by computer-controlled potentiostat–galvanostat (potentiostat - galvanostat IPC – PRO (Volta LLC, Russia)) at room temperature. Cyclic voltammetry (CVA) and linear sweep voltammetry (LSV) measurements were performed at 0.001–0.3 V/s range of potential scan rates and electrode potential window of −1.1 — +1.6 V. Electrode potentials were registered and shown below in comparison to Ag/AgCl, KCl (saturated) reference electrode (SSCE). The electrolyte containing 0.3 M LiOH was saturated with oxygen 30 min before each experiment.

Carbon paste electrode (CPE) was assembled to study manganese dioxide samples electrocatalytic activity in ORR&OER. CPE was a thoroughly grounded mixture of doped manganese dioxide: graphite in 70:30 ratio and polytetrafluoroethylene (PTFE) emulsion (S = 0.045 cm^2) placed into a silicone tube with metallic collector inside supplied with the Luggin capillary. Three electrode cell contained also a glass–carbon plate auxiliary electrode and silver/silver chloride reference electrode. The OER/ORR process' currents were taken as currents of corresponding linear sections of CVA curves in semilogarithmic Tafel coordinates. Preliminary cycling was applied to achieve reproducible CVA curves of the working electrode surface. Before the final cycles at 0.02 V/s, several steps of cycling at higher scan rates were performed.

Table 1
Additives (mol/L) to the pristine electrolyte 0.7 M $MnSO_4$ and 0.1 M HF.

Sample	Introduced additives (mol/L)		
	$(NH_4)_2SO_4$	$FeSO_4$	$CoSO_4$
1	1.5	0.01	0.01
2	1.5	0.01	0.1
3	1.5	0.1	0.01
4	–	0.01	0.1
5	–	0.1	0.1
6	1.5	–	–

3. Results and discussion

3.1. Synthesis of NH_4^+, Fe^{2+}, Co^{2+}-doped EMDs

Six experimental samples have been obtained (Table 1). One of them was electrodeposited from the electrolyte with a composition of 0.1 M HF, 0.7 M $MnSO_4$, 1.5 M $(NH_4)_2SO_4$. It was accepted as a standard one comparing with doped by Fe^{2+}, Co^{2+} samples. The current yields were evaluated. The values of yield were 77.47, 62.18, 51.59, 40.1, 10.9 % for samples 1–5, respectively. The higher dopant cations Fe^{2+} and Co^{2+} concentration in an electrolyte, the lower current yield of electrodeposition product.

3.2. Thermogravimetry study and atomic absorption spectroscopy

Temperature range of 20–1000 °C in thermogravimetric study included the formation of thermodynamically more stable Mn_2O_3, Mn_3O_4, and MnO. This range allows to assess the chemical composition of the samples in combination with AAS data more accurately. Losses up to 500 °C were applied to assess the concentration of point defects and the content of surface and bulk OH-groups in samples. An example of a derivatogram of sample 2 is presented in Fig. 1.

The total water and OH - groups content was estimated as the mass loss in the temperature range 21–490 °C. This content is varied between 2.79 and 9.57% for samples 1, 2, 4, 5 but the maximal value of 15.57% was observed in sample 3. Surface water and OH-groups content is in the range of 1.01–10.20 mas. %. The content of hydroxide groups was found by DTG curve effects in the range 150–490 °C. The endothermic effects can be observed on the DTA curves of the studied samples at the following temperature ranges of 21–245, 156–288, 250–470, 450 – 620, and 810–965 °C. The effects at the beginning of the heat treatment process include the loss of physically sorbed water. The effects at 156–288 °C are less pronounced and characterize the loss of chemisorbed water on the inhomogeneities of the near-surface layers, as well as the beginning of the removal of surface hydroxide groups [21]. The bulk hydroxide groups loss occurs up to 490 °C. The weak exoeffect at 313–392 °C and subsequent change in the slope of the DTA curve may correspond to complete dehydration of MnO_2 and phase tran-

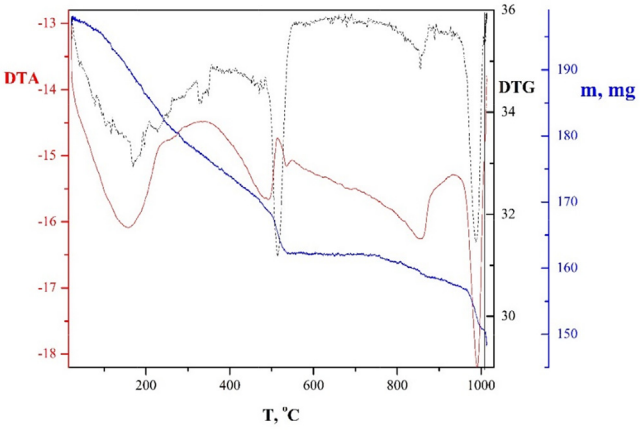

Fig. 1. Thermogravimetric curves of DTA, DTG and TG for sample 2.

sition γ-MnO_2 → β-MnO_2 for γ-phase samples [22]. The absence of shoulder-shaped peaks on the DTG curve for effects at 470–620 °C indicates a one-stage transition MnO_2 → Mn_2O_3, without the formation of Mn_5O_8 [23].

The chemical formula was calculated for each sample (Table 2) using AAS and TGA data. This formula was introduced in P. Ruetschi's cationic vacancies model [24]:

$$Mn^{4+}_{1-x-y}Mn^{3+}_{x}\ y\ O_{2-x-4y}OH_{4y+x}$$

where x and y are molar fractions of Mn^{3+} and cationic vacancies (□), respectively. The result of the calculation for sample 3 is completely consistent with the data published in [25].

The presence of Mn^{3+} with the admixture of Mn^{4+} is a key to achieve high specific ORR activities in perovskites [26]. Previous findings [27] have shown that having Mn valence slightly above 3+ can provide the highest specific ORR activities found for perovskite oxides (mixed with AB carbon) in alkaline solution. Ryabova et al indicated that Mn^{3+} oxides are more active ORR electrocatalysts [28]. Thus, enhancement of ORR activity is expected for containing Mn^{3+} samples.

3.3. X-ray diffraction analysis and FTIR-spectroscopy of electrolytically doped by cations Fe^{2+}, Co^{2+}, NH_4^+ -MnO_2 samples

Normalized XRD patterns of studied samples are shown in Fig. 2, a. FTIR-spectra in fingerprint region below 1000 cm^{-1} allow also to distinguish phases in nanocrystallites where XRD application is limited (Fig. 2, b). Standard sample of doped with NH_4^+-ions EMD of predominately hollandite phase is taken for comparison purposes. It can be clearly seen that sample 3 has distinct features. Chemical analysis together with XRD, DTA-data confirmed formation of MnOOH-phase at maximal Fe^{2+} electrolyte concentration (0.1 M Fe^{2+}) in this work. As a result of destructive influence of Co^{2+}- and Fe^{2+}-additives, hollandite phase peaks at low 2theta angles are suppressed. The short range order features of hollandite remain similar to Sample 6 for samples 1, 2 as shown in Fig. 2, b. Sample 3 demonstrates significant differences. The shift of the 2-theta peak at 10.5 degrees of the minor ramsdellite phase component of sample 4 to lower 2theta region confirms enlargement of the unit cell and formation of larger in size structure of Mn^{3+} in MnOOH. To summarize observed XRD- and FTIR-effects, Co^{2+}- and Fe^{2+}-additives decrease the size of hollandite phase crystallites. Combining this finding with SEM observation of disappearance of hollandite nanorods and nanowires (see below) and drop in the current yield of doped samples, it can be concluded that ramsdellite formation pathway has a favor due to isomorphic α-Mn^{3+}OOH groutite structure (space group Pnma and unit-cell parameters a = 4.55–4.56, b = 10.47–10.70, c = 2.87 Å; Z = 4 [29]) stabilization at the presence of additives.

Groutite is also isostructural to goethite FeOOH and forms an isomorphous series with ramsdellite MnO_2. It is also evident that Fe^{3+}/Fe^{2+} redox pair is a source of parasitic currents on electrodes. There is also growth of 13.0 2theta degree peak in sample 3. It could be attributed to manganite β-MnOOH as the next distorted derivative of pyrolusite β-MnO_2.

These results are consistent with the behavior of heavy doped by Co^{2+} and Li^+-ions series of samples in [18] where the ending member of the doping series with Co^{2+}-content close to about 2% was semiamorphous sample with isomorphous to ramsdellite hetoregenite CoOOH structure. The hollandite ammonium based formation pathway loses its thermodynamic advantages since hollandite structure cannot support so high content of low valenced manganese. Samples 4, 5 obtained from ammonium-free electrolyte have typical disordered ramsdellite like XRD-patterns, semiamorphous in case of sample 5.

3.4. SEM and BET surface studies

SEM experiment was combined with EDS analysis of the area of interest. EDS results were generally consistent with discussed above AAS and TGA data. The shape of nanocrystallites and morphology of their aggregates is shown in Fig. 3. Samples exhibit the variety of nanoparticles morphology including nanoneedles and nanowires (Fig. 3 a,b). Lamellar aggregates with thickness of 1–2 μm were also a common feature of all samples at the electrodeposition conditions used in this work (Fig. 3, images at lower, 19,300 times, magnification).

Nanoneedles and nanowires are typical for electrodeposition product aggregates in Samples 1–2 (Fig. 3 a,b). The distinctive feature of sample 3 morphology (Fig. 3, c) is poor crystallization of aggregates with rare and short nanoneedle crystallites visible in the field of view, which is consistent with disappearance of hollandite phase peaks on XRD-patterns and the fact that iron additives decrease the current yield of electrodeposition. Fig. 3 d, e display SEM images of samples 4 and 5 synthesized from ammonium free electrolytes (NH_4^+ as a template of hollandite phase was discussed in [3]). Sample 4 consists mostly of lamellae. It was one of the most important EDS-findings that cobalt of this sample is concentrated only in cavities inside lamellae containing aggregated crystallites of more regular shape with a dimension of about 50 × 50 nm; cross-sections due to cobalt incorporation are crumbly (Fig. 3, d). The expected cobalt accumulation mechanism was discussed in [4]. Sample 5 is represented by lamellar macroaggregates covered with spheres of about 300 nm in diameter. This sample has the largest size of aggregates, the densest both visually and when grinding in an agate mortar after electrodeposition and drying.

Since both ORR and OER are surface processes the electrocatalyst morphology plays an important role in electrocatalytic performance. As shown by C. Julien [30] and N. Ivanova [31], poor transport properties of a bulk material are typically responsible for poor electrochemical performance due to low electronic and ionic conductivities. The characteristic time for electronic species to reach the surface of a fixed dimension can be significantly reduced in case of application of a catalyst with nanosized particles. Simultaneously, the surface area of this material grows that reduces the resistance of the catalyst [31].

Table 2
Chemical analysis, calculated according to the cationic vacancies model formula, and BET surface area of samples 1–6.

Sample	Elemental analysis, mass. %			Chemical formula	S_{BET}, m^2/g
	Mn	Fe	Co		
1	51.46	0.31	0.22	$Mn^{4+}_{0.83}Mn^{3+}_{0.02}\square_{0.15}Co_{0.007}Fe_{0.01}O_{1.38}OH_{0.62}$	208.4
2	50.61	0.22	0.80	$Mn^{4+}_{0.63}Mn^{3+}_{0.34}\square_{0.03}Co_{0.027}Fe_{0.008}O_{1.53}OH_{0.47}$	157.8
3	35.21	2.91	0.15	$Mn^{4+}_{0.13}Mn^{3+}_{0.57}\square_{0.3}Co_{0.005}Fe_{0.1}O_{0.23}OH_{1.77}$	18.0
4	49.40	6.63	0.354	$Mn^{4+}_{0.91}Mn^{3+}_{0.05}\square_{0.04}Co_{0.027}Fe_{0.009}O_{1.79}OH_{0.21}$	303.7
5	65.43	0.249	0.781	$Mn^{4+}_{0.42}Mn^{3+}_{0.46}\square_{0.12}Co_{0.012}Fe_{0.236}O_{1.06}OH_{0.94}$	57.7
6	51.89	–	–	$Mn^{4+}_{0.84}Mn^{3+}_{0.04}\square_{0.12}O_{1.48}OH_{0.52}$	138.0

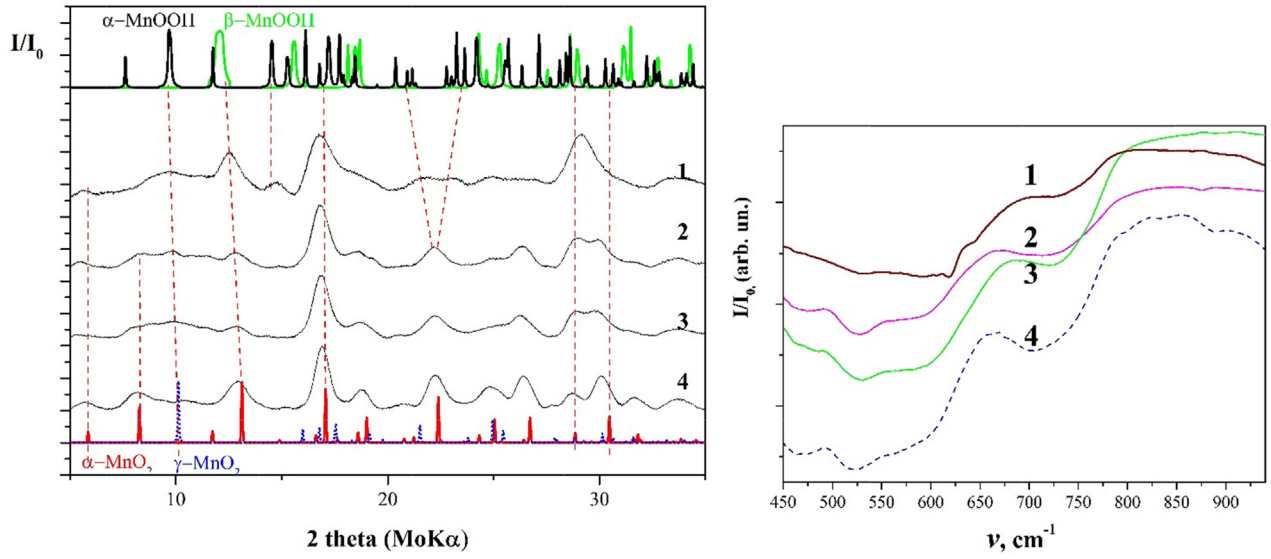

Fig. 2. X-ray phase analysis (a) and FTIR spectroscopy (b) of samples 1(curve 3); 2(curve 2); 3(curve 1); 6(curve 4).

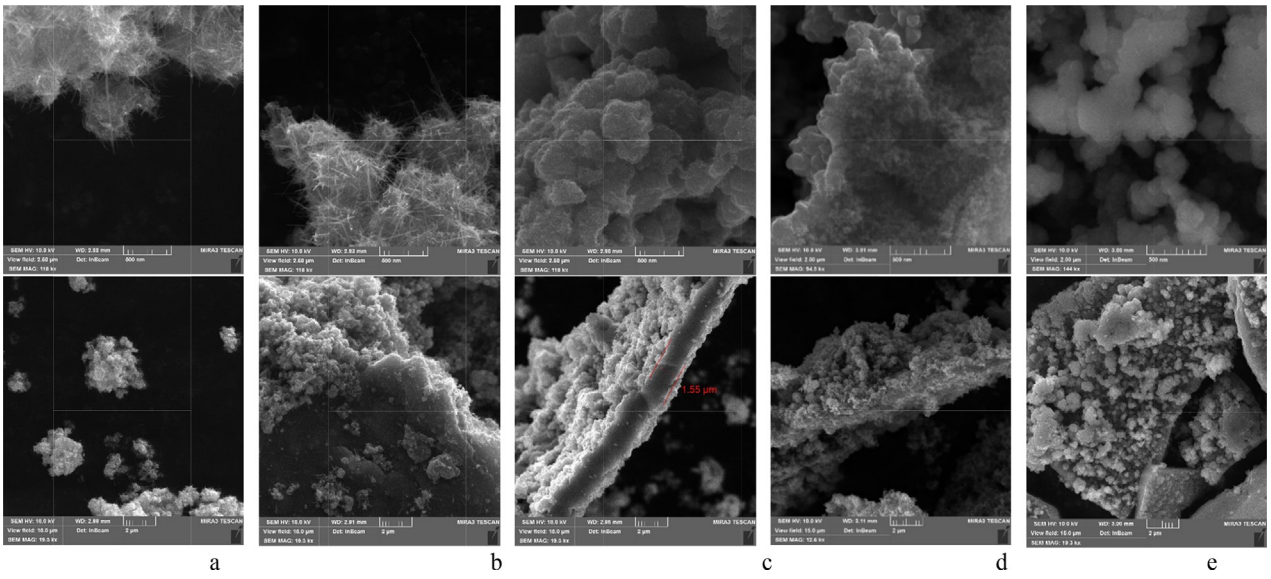

Fig. 3. SEM images of samples 1–5 with identical magnifications (a — e, scale bars are 2000 and 500 nm).

Surface area BET data are demonstrated in Table 2. It is evident that changes in morphology in Fig. 3 are not in line with complex behaviour of surface area in Samples 1–6. For instance, Sample 5 with the largest aggregates (Fig. 3, d) has maximal surface area. Phase composition including micropores of hollandite phase structure tunnels and semiamorphous Sample 5 contribute to surface area.

3.5. OER/ORR parameters correlations in Fe^{2+} and Co^{2+}-doped manganese dioxides

Electrocatalytic activity is a function of active centres onto oxide material surface that include defect positions of a host structure as well as positions of incorporated dopant ions [32,33]. The influence of polycationic doping by NH_4^+, Fe^{2+}, Co^{2+}-ions of manganese dioxide on the kinetic parameters of ORR (OER) processes was studied. Correlations of ORR/OER activity with such structure parameters as the content of cationic vacancies, molar Mn^{3+}/Mn^{4+} ratio, and dopant ion concentration were analysed (Fig. 4).

Correlations of electrode potentials at the same current densities of the anode CVA curve in OER region are shown for doped samples in Fig. 4, a. The potential is decreased when the content of Fe and Co demonstrate an increase (Samples 1–3). The same trend is observed for the current density peaks, i_{pa}, of OER process. Samples 4,5 belong to another series synthesized from ammonium-free electrolyte and demonstrate less evident but sometimes different response. For instance, despite the same content of dopant ions in the electrolyte and identical total content of Fe and Co in the electrodeposition product with Sample 2 (ammonium electrolyte), Sample 4 shows comparable values of a potential with sample 2 at 5 mA/cm^2, and at higher current densities, overpotential of the anode process increases significantly. Sample 5 behaviour is similar to Sample 4 with a little bit lower potentials (Fig. 4, a).

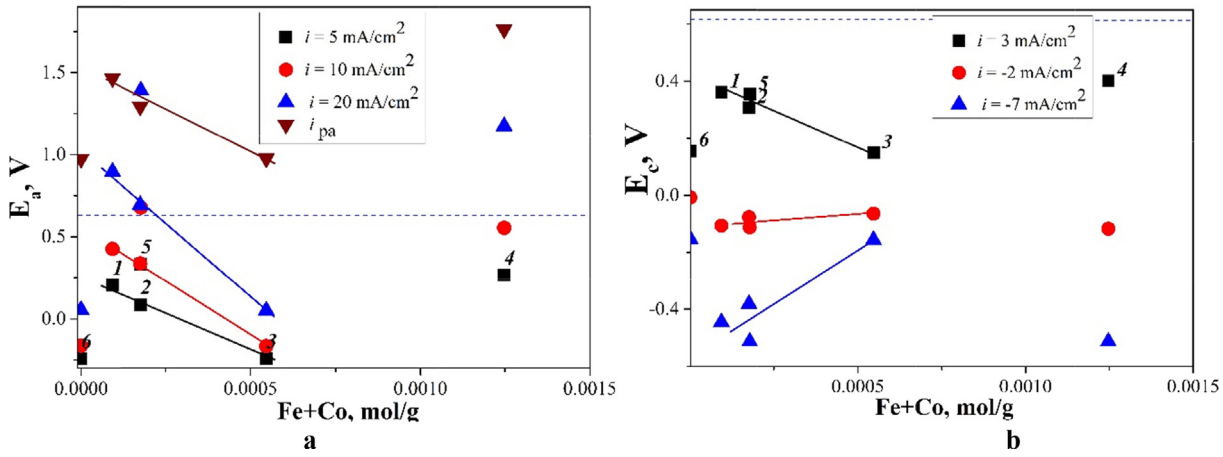

Fig. 4. Correlations of electrode potentials at i = 5, 10, 20 mA/cm^2, and i_{pa} (OER peak current density) of anode CVA-curve (a) and at i = 3, −2, −7 mA/cm^2 of cathode CVA-curve (b) with the total Fe and Co content (mol/g). Numbers of samples 1–6 are also shown, the dashed blue line indicates equilibrium oxygen electrode potential at the conditions studied (0.627 V). (For interpretation of the references to colour in this figure legend, the reader is referred to the web version of this article.)

The correlations of potentials in ORR region at the same current densities of the cathode CVA branch is shown for a series of samples doped with ammonium (Fig. 4, b). There is a decrease in ORR overpotential with the growth of dopant ions concentration in the series of samples 1–3, 5. Sample 4 is out of the aforementioned correlation with the total content of dopant ions Fe and Co. However, it demonstrates comparable ORR overpotential with Sample 4 of the same ammonium-free series. It can be assumed that the surface active centres concentration of dopant ions is approximately the same for samples 4, 5. It is reasonable hypothesis since our SEM&EDS data confirm some accumulation of cobalt inside of lamellae crystallytes for Samples 4,5. The excess of iron content is probably attributed to the bulk states also since isomorphous series of α-, β-MnOOH with goethite FeOOH could be responsible for these bulk states of iron in sample 5 and its semi-amorphous state. It becomes evident if to compare the growth by about 2 times of Fe content in Sample 5 regarding Sample 3 at identical Mn^{3+}-content (see Table 2). It should be added that both samples had the same (0.1 M) Fe^{2+} concentration in the electrolyte.

Sample 6 with hollandite structure main phase component together with sample 3 demonstrate rather ORR then OER activity in terms of overpotential in comparison with equilibrium oxygen electrode potential (see Fig. 4). Conditions of our CVA experiment were far from the thermodynamic equilibrium but the latter oxygen electrode potential was used for comparison purposes. As can be seen in Fig. 4, even the low additive of Fe^{2+}, Co^{2+} concentration (0.01 M) causes a drastic change in ORR/OER behaviour of studied samples (see the difference for Sample 1 and Sample 6). Probably dopant ions further control overpotential behaviour of the samples (See correlations in Fig. 4). Thus, analysing correlations in Fig. 4, the following generalisation is possible: dopant Fe- and Co-ions of less than $6{\cdot}10^{-4}$ mol/g content in the doped samples 1–3, 5 demonstrate a positive effect both on OER and ORR overpotential. Overpotentials for ORR (V) at − 0.1 mA/cm^2 of samples 1, 2 were evaluated as 0.539 V; 3 as 0.570 V; 4,5 as 0.554 V that are comparable with presented in [7] overpotential data for manganese oxides.

The analysis of linear ORR/OER sections of the Tafel plots for doped samples is also useful. Results for two linear ORR regions where the following: the number of electrons for the first region was evaluated as n = 4 and for the second region it was evaluated as 1. The average value of the transfer coefficient for all processes is 0.5. Therefore, it was suggested that n = 4 is the predominant mechanism of the direct ORR 4e$^-$ pathway [34].

Our task was also to assess the most promising samples in terms of bifunctionality in ORR/OER. The following graphical representation was proposed for this purpose: current densities per geometrical and BET surface areas of $ORR_{1,2}$ (Fig. 5, a); $OER_{1,2}$ (Fig. 5, b); $OER_{1,2}$&$ORR_{1,2}$ (Fig. 5, c) sections of Tafel plots of studied samples were taken together with an overpotential of ORR_1, OER_1, and ORR_1&OER1, respectively. The idea was to estimate the effects of doping on anode and cathode processes efficiency as well as to check bifunctionality as a criterium of maximal current density at minimal overpotential.

It can be seen for current densities per geometrical surface area (Fig. 5, c) that the maximal total current at minimal overpotential is inherent to sample 2. Sample 3 is comparable with sample 2 in the total current density but has maximal overpotential among other samples. The pristine sample 6 without Co^{2+}&Fe^{2+}additives has the advantages of minimal overpotential in both OER&ORRs. The exceptional by 3–4 times larger current densities per BET surface area demonstrates sample 3 in Fig. 5. The significant differences of Sample 3 parameters we attribute to maximal content of Mn^{3+} having both oxidising and reducing properties as well as MnOOH structure. The difference in Mn^{3+} content in Samples 3 and 5 can suggest the role of ammonium-ions as ligands stabilizing Mn^{3+} at electrodeposition. The lowest surface area in this sample is the result of reducing properties of 0.1MFe^{2+} at the presence of NH_4^+.

As shown in [36] for synthetic hollandite samples, the best ORR performing catalyst was that with the higher surface water content (associated to material BET surface area) and a (3 1 0) surface as the 2nd more contributing plane (after 211). On the other hand, the catalyst with the higher structural water and with (1 1 0) and (2 0 0) crystallographic planes being the most intensity contributors (after 211) was the most OER active material. In this work, aforementioned observations were fair only partially since samples have different phase composition (hollandite, ramsdellite, α-Mn^{3+}OOH groutite, β-Mn^{3+}OOH, and amorphous phases) and doping effects are significant. As shown in Valim et al paper [37], the superior performance of α-MnO_2 is attributed to the existence of different surface concentrations of Mn^{3+} ions, whose are supposedly higher and more accessible in this species than on the other allotropic forms of manganese dioxide.

Among hollandite containing Samples 1, 2, 6, (3 1 0) peak was the most intensive after (2 1 1) peak for sample 6 having the better ORR current densities than Samples1 and 2. Unfortunately, water content evaluated from DTA in this study had no correlations with the surface area and electrocatalytic activity.

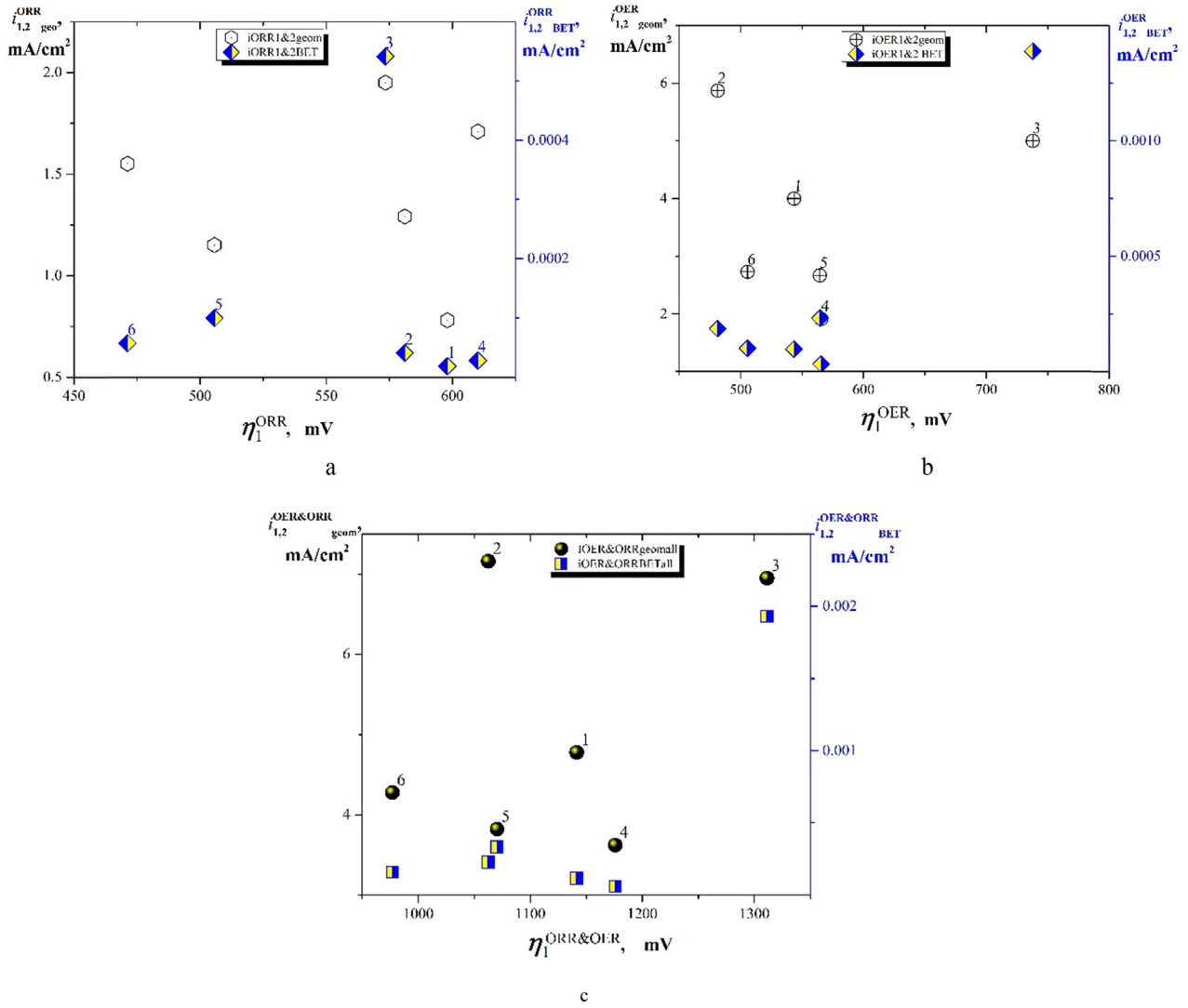

Fig. 5. Current densities per geometrical and BET surface areas of $ORR_{1,2}$(a); $OER_{1,2}$ (b); $OER_{1,2}$&$ORR_{1,2}$ (c) sections of Tafel plots of studied samples versus overpotential of ORR_1, OER_1, and ORR_1&OER1, respectively.

The ratio of intensities of hollandite peaks as a correlation parameter with electrocatalytic ORR/OER activity is difficult to expect since it is the bulk property. Nevertheless, the hollandite structure has tunnels with properties of molecular sieves (with about 0,5 nm diameter). The planes (110) and (200) describe the cross-section of these tunnels but their availability and capacity by molecules of water depends on another guest ions and their distribution inside tunnels. There is also problem of material design with special pore's distribution by size and volume to make them available for transport of reagents and products. In this case, we expect also the correlation of the relative intensity of (110) and (200) peaks with OER reaction activity. The unknown factor of influence here is that electrodeposition of MnO_2 in an aqueous electrolyte is attended by OER process.

4. Conclusions

The interrelationship of ORR & OER and structure (i.e. concentration of dopants, OH-groups, Mn^{3+}, cationic vacancies etc.) parameters is complex. The change of phase composition in samples depending on the content of dopants of Co^{2+}, Fe^{2+}, and NH_4^+ is an additional factor of influence. The typical phase components in co-doped in this work EMDs were hollandite, ramsdellite, amorphous phase, as well as $Mn^{3+}OOH$ probably with isomorphous substitution by Fe^{3+}. As shown above, Co^{2+} is accumulated in the bulk but our previous findings in [4,35] showed the accompanying growth of cationic vacancies and microtwinning at monodoping by Co^{2+} of EMDs. SEM images demonstrated pathways of cobalt incorporation on image with a crumbly cross-section of lamellar aggregates with the thickness of 1–2 μm (Fig. 3 d). The possible mechanism of such incorporation was suggested in [3]. The role of cationic vacancies and surface water content remains unclear from our data. Nevertheless, the positive influence of Mn^{3+} content and phases of MnOOH formed mostly due to the reducing activity of Fe^{2+}-dopant are evident.

Dopant-ions of Fe and Co content below $6{\cdot}10^{-4}$ mol/g decrease the overpotential of ORR&OER as established by the existing correlations of ORR & OER potentials at the same current density with Fe + Co content in EMD samples. Analysis of the maximal value of total current density at minimal overpotential of ORR + OER makes it possible to identify the best bifunctional electrocatalysts for both ORR & OER reactions. The best in our work bifunctionality of Sample 2 could be attributed to its large surface area and optimal combination of phases (hollandite, ramsdellite, amorphous

component with low content of Mn^{3+}-phase), the definite surface concentration of dopant ions, and defect states the latter responsible for. As shown by chemical analysis data, there is accompanied by the growth of dopants concentration increase of Mn^{3+}-content in samples. MnOOH phase based sample with maximal content of Mn^{3+} (Sample 3) demonstrated the maximal total current density of ORR&OER vs BET surface but it has the maximal overpotential simultaneously. Hollandite sample 6 doped by only NH_4^+-ions as templates of hollandite structure tunnels has minimal overpotential among ramsdellite-like materials (Samples 4–5), defected hollandite (Samples 1–2), MnOOH phase based sample (Sample 3).

To sum up the results obtained, the hollandite phase (NH_4^+-ions doping) favours minimal overpotential of both OER/ORR but, especially, Mn^{3+} in hollandite(Samples 2,6), distorted ramsdellite-like semiamorphous Sample 5 up to MnOOH (Sample 3) increases the ORR/OER current densities. MnOOH phases demonstrate the highest specific ORR/OER current density per BET surface area. Generally, the surface area effects are complex in the series of electrodeposited manganese oxide/hydroxides studied. The role of micropores as structure channels of hollandite is probably a key factor in the lowest overpotential of hollandite-like samples. The optimal combination of doping parameters needs further study to improve the bifunctionality of electrodeposited manganese oxides.

CRediT authorship contribution statement

Luiza Zudina: Investigation, Data curation, Writing – original draft. **Georgii Sokolsky:** Supervision, Investigation, Data curation, Writing – review & editing. **Vitalii Chumak:** Formal analysis, Methodology. **Nadiia Haiuk:** Visualization, Investigation.

Declaration of Competing Interest

The authors declare that they have no known competing financial interests or personal relationships that could have appeared to influence the work reported in this paper.

Acknowledgements

Authors are grateful to Mykola Tsiba (Institute for Sorption and Problems of Endoecology NAS of Ukraine) for valuable help with surface area measurements despite difficult times.

Appendix A. Supplementary material

Supplementary data to this article can be found online at https://doi.org/10.1016/j.matpr.2022.05.570.

References

[1] P. Wang, Y. Lin, L. Wan, B. Wang, Construction of a Janus MnO_2-NiFe Electrode via Selective Electrodeposition Strategy as a High-Performance Bifunctional Electrocatalyst for Rechargeable Zinc-Air Batteries, ACS Appl. Mater. Interfaces 11 (41) (2019) 37701–37707, https://doi.org/10.1021/acsami.9b12232.
[2] S. Chou, F. Cheng, J. Chen, Electrodeposition synthesis and electrochemical properties of nanostructured γ-MnO_2 films, J. Power Sources 162 (2006) 727–734, https://doi.org/10.1016/j.jpowsour.2006.06.033.
[3] G. Sokolsky, B. Ye, N. Ivanova, S. Ivanov, G. Kolbasov, G. Lazzara, L. Zudina, N. Gayuk, S. Chivikov, Effects of electrolyte doping on electrodeposited nanostructured manganese oxide and chromium oxide, Surface Coatings Technol. 400 (2020), https://doi.org/10.1016/j.surfcoat.2020.126211.
[4] G. Sokolsky, L. Zudina, E. Boldyrev, O. Miroshnikov, N. Gauk, O. Kiporenko, ORR electrocatalysis study by Cr^{3+}, Fe^{2+}, Co^{2+} -doped manganese(IV) oxides, Acta Phys. Pol. A 133 (2018) 1097–1102, https://doi.org/10.12693/APhysPolA.131.1097.
[5] A.M. Hashem, A.M. Abdel-Latif, H.M. Abuzeid, H.M. Abbas, H. Ehrenberg, R.S. Farag, A. Mauger, C.M. Julien, Improvement of the electrochemical performance of nanosized α-MnO_2 used as cathode material for Li-batteries by Sn-doping, J. Alloy. Compd. 509 (2011) 9669–9674, https://doi.org/10.1149/05024.0125ecst.
[6] M. Wang, K. Chen, J. Liu, Q. He, G. Li, F. Li, Efficiently Enhancing Electrocatalytic Activity of α-MnO_2 Nanorods/N-Doped Ketjenblack Carbon for Oxygen Reduction Reaction and Oxygen Evolution Reaction Using Facile Regulated Hydrothermal Treatment, Catalysts 8 (4) (2018) 138.
[7] J.H. Siow, M.R. Bilad, W. Caesarendra, J.J. Leam, M.A. Bustam, N.S. Sambudi, Y. Wibisono, T.M.I. Mahlia, Progress in Development of Nanostructured Manganese Oxide as Catalyst for Oxygen Reduction and Evolution Reaction, Energies 14 (19) (2021) 6385.
[8] M. Yin, H.e. Miao, H.u. Ruigan, Z. Sun, H. Li, Manganese dioxides for oxygen electrocatalysis in energy conversion and storage systems over full pH range, J. Power Sources 494 (15) (May 2021), https://doi.org/10.1016/j.jpowsour.2021.229779 229779.
[9] C. Song, J. Zhang, in: J. Zhang (Ed.). PEM Fuel Cell Electrocatalysts and Catalyst Layers: Fundamentals and Applications, Springer, London, 2008, pp. 89. https://doi.org/10.1007/978-1-84800-936-3. https://doi.org/10.3390/catal8040138.
[10] P.M. De Wolff, Interpretation of Some γ-MnO_2 Diffraction Patterns, Acta Crystall. 12 (1959) 341–345, https://doi.org/10.1107/s0365110x59001001.
[11] N.D. Ivanova, E.I. Boldurev, I.S. Makeeva, G.V. Sokolsky, Obtaining manganese dioxide from fluorine-containing electrolytes, Jurn. Prykl. Chem. 71 (1998) 1211, ISSN 0321 - 4095.
[12] P. Pei, K. Wang, Z. Ma, Technologies for Extending Zinc-Air Battery's Cyclelife: A Review, Appl. Energy 128 (2014) 315–324, https://doi.org/10.1016/j.apenergy.2014.04.095.
[13] Y. Li, H. Dai, Recent Advances in Zinc-Air Batteries, Chem. Soc. Rev. 43 (2014) 5257–5275, https://doi.org/10.1039/C4CS00015C.
[14] T.R. Ralph, M.P. Hogarth, Catalysis for Low Temperature Fuel Cells, Platin. Met. Rev. 46 (2002) 117–135.
[15] P. Bruce, B. Scrosati, J.-M. Tarascon, Nanomaterials for Rechargeable Lithium Batteries, Angew. Chem. 79 (2008) 120–132, https://doi.org/10.1002/anie.200702505.
[16] G.V. Sokol'skii, S.V. Ivanova, N.D. Ivanova, E.I. Boldyrev, T.F. Lobunets, T.V. Tomila, Doped manganese (IV) oxide in processes of destruction and removal of organic compounds from aqueous solutions, J. Water Chem. Technol. 34 (5) (2012) 227–233.
[17] G.V. Sokolsky, S.V. Ivanov, N.D. Ivanova, Y.I. Boldurev, O.V. Kobulinskaya, M.V. Demchenko, Cobalt Additives Influence on Phase Composition and Defect Structure of Manganese Dioxide Prepared from Fluorine Containing Electrolytes, Acta Phys. Pol. A 117 (1) (2010) 86–90.
[18] G. Sokolsky, N. Ivanova, S. Ivanov, T. Tomila, Y.e. Boldyrev, Phase composition and crystallinity degree of nanostructured products of anode oxidation of manganese(II) ions doped by ions of lithium and cobalt(II), Sci Sintering 39 (3) (2007) 273–279.
[19] M. Xiong, D.G. Ivey, J. Electrochem. Soc. 164 (2017) A1012–A1021, https://doi.org/10.1149/2.0481706jes.
[20] G. Sokolsky, S. Ivanov, N. Ivanova, Ye. Boldyrev, M. Kakazey, Materials Today Virtual Conference on Nanotechnology (December 13—15, 2012).
[21] C.C. Lee, C.E. Newnham, F.S. Stone, F.L. Tye, Temperature programmed desorption studies on -phase manganese dioxide in static water vapor environments, J. Colloid Interface Sci. 45 (2) (1973) 289–294, https://doi.org/10.1016/0021-9797(73)90269-5.
[22] P. Špičák, M. Sedlaříková, M. Zatloukal, V. Novák, J. Kazelle, J. Vondrák, J. Sol. St. Electrochem. (2010), https://doi.org/10.1007/s10008-010-1198-2.
[23] M.I. Said, B. Harbrecht, Controlled synthesis of Mn_5O_8 and β-MnO_2 nanorods via thermal decomposition of γ-MnOOH precursor: Characterization and magnetic properties of Mn_5O_8, J. Alloys Comp 710 (2017) 635–643, https://doi.org/10.1016/j.jallcom.2017.03.138.
[24] P. Ruetschi, Cation-Vacancy Model for MnO_2, J. Electrochem. Soc. 131 (12) (1984) 2737–2744.
[25] C.M. Julien, M. Massot, C. Poinsignon, Spectrochim. Acta Part A Mol. Biomol. Spectrosc. 60 (3) (2004) 689, https://doi.org/10.1016/S1386-1425(03)00279-8.
[26] K.A. Stoerzinger, M. Risch, B. Han, Y. Shao-Horn, Recent Insights into Manganese Oxides in Catalyzing Oxygen Reduction Kinetics, ACS Catal. 5 (10) (2015) 6021–6031.
[27] J. Suntivich, H.A. Gasteiger, N. Yabuuchi, H. Nakanishi, J.B. Goodenough, Y. Shao-Horn, Nat. Chem. 3 (2011) 546–550, https://doi.org/10.1038/nchem.1069.
[28] A.S. Ryabova, F.S. Napolskiy, T. Poux, S.Y. Istomin, A. Bonnefont, D. Antipin, A.Y. Baranchikov, E. Levin, A.M. Abukamov, G. Kéranguéven, E.V. Antipov, G.A. Tsirlina, E.R. Savinova, Rationalizing the Influence of the Mn(IV)/Mn(III) Red-Ox Transition on the Electrocatalytic Activity of Manganese Oxides in the Oxygen Reduction Reaction, Electrochim. Acta. 187 (2016) 161–172, https://doi.org/10.1016/j.electacta.2015.11.012.
[29] N.V. Chukanov, D.A. Varlamov, I.V. Pekov, N.V. Zubkova, A.V. Kasatkin, S.N. Britvin, Coupled Substitutions in Natural MnO(OH) Polymorphs: Infrared Spectroscopic Investigation, Minerals 11 (2021) 969, https://doi.org/10.3390/min11090969.
[30] C. Julien, A. Mauger, Nanostructured MnO_2 as Electrode Materials for Energy Storage, Nanomaterials 7 (2017) 396, https://doi.org/10.3390/nano7110396.
[31] N.D. Ivanova, E.I. Boldyrev, G.V. Sokol'skii, I.S. Makeeva, Composition, properties, and electrochemical behavior of nonstoichiometric manganese dioxide obtained in fluoride-containing electrolytes, Russ. J. Electrochem. 38 (9) (2002) 981–986, https://doi.org/10.1023/A:1020288927771.

[32] P.H. Benhangi, A. Alfantazi, E. Gyenge, Doped MnO_2-Based Oxygen Reduction and Evolution Catalysts for Bifunctional Cathodes in Alkaline Electrochemical Power Sources, in: Proceedings of the 224th ECS Meeting, San Francisco, CA, USA. 2013.
[33] I.M. Mosa, S. Biswas, A.M. El-Sawy, V. Botu, C. Guild, W. Song, R. Ramprasad, J.F. Rusling, S.L. Suib, Tunable mesoporous manganese oxide for high performance oxygen reduction and evolution reactions, J. Mater. Chem. A 4 (2) (2016) 620–631.
[34] Y.L. Cao, H.X. Yang, X.P. Ai, L.F. Xiao, The mechanism of oxygen reduction on MnO_2-catalyzed air cathode in alkaline solution, J. Electroanal. Chem. 557 (2003) 127–134, https://doi.org/10.1021/acs.inorgchem.9b00492.
[35] G. Sokolsky, S. Ivanov, E. Boldyrev, N. Ivanova, L. Vasylechko, Toward stimulated by defects functionality in manganese (IV) oxide materials, in: International Conference on Oxide Materials for Electronic Engineering-fabrication, properties and applications (OMEE-2014), IEEE, 2014, pp. 49–50, https://doi.org/10.1109/OMEE.2014.6912334.
[36] A.R. Mainar, L.C. Colmenares, O. Leonet, F. Alcaide, J.J. Iruin, S. Weinberger, V. Hacker, E. Iruin, I. Urdanpilleta, J.A. Blazquez, Manganese oxide catalysts for secondary zinc air batteries: from electrocatalytic activity to bifunctional air electrode performance, Electrochim. Acta 217 (2016) 80–91.
[37] R.B. Valim, M.C. Santos, M. Lanza, S.A.S. Machado, F. Lima, M.L. Calegaro, Oxygen reduction reaction catalyzed by ε-MnO2: influence of the crystalline structure on the reaction mechanism, Electrochim. Acta 85 (2012) 423–431, https://doi.org/10.1016/j.electacta.2012.08.075.